JGR Planets

RESEARCH ARTICLE
10.1029/2024JE008826

Key Points:

- The SHERLOC instrument is capable of detecting minerals and organics in martian meteorites
- Raman shows differences between original martian organic material and material from terrestrial weathering
- We detected fluorescence from both organic material and trace cerium present in igneous phosphate grains

Supporting Information:

Supporting Information may be found in the online version of this article.

Correspondence to:

J. Razzell Hollis,
j.razzellhollis@gmail.com

Citation:

Razzell Hollis, J., Moore, K., Fries, M., Broderick, C., Buret, Y., Bhartia, R., et al. (2025). Mineralogical and chemical mapping of Martian meteorite SaU 008 using deep UV Raman and fluorescence spectroscopy on Earth and Mars. *Journal of Geophysical Research: Planets*, *130*, e2024JE008826. https://doi.org/10.1029/2024JE008826

Received 28 OCT 2024
Accepted 21 JUL 2025

Author Contributions:

Conceptualization: Joseph Razzell Hollis
Data curation: Joseph Razzell Hollis, Marc Fries
Formal analysis: Joseph Razzell Hollis, Kelsey Moore
Funding acquisition: Joseph Razzell Hollis
Investigation: Joseph Razzell Hollis, Kelsey Moore, Cindy Broderick, Yannick Buret
Methodology: Joseph Razzell Hollis, Kelsey Moore
Project administration: Kevin P. Hand, Kyle Uckert

Mineralogical and Chemical Mapping of Martian Meteorite SaU 008 Using Deep UV Raman and Fluorescence Spectroscopy on Earth and Mars

Joseph Razzell Hollis[1,2], Kelsey Moore[2,3], Marc Fries[4], Cindy Broderick[1], Yannick Buret[1], Rohit Bhartia[5], Teresa Fornaro[6], Trevor Graff[7], Kevin P. Hand[2], Keyron Hickman-Lewis[8], Ryan Jakubek[4], Carina Lee[7,9], Francis M. McCubbin[4], Richard V. Morris[10], Ashley Murphy[11], Sunanda Sharma[12], Caroline Smith[1], Andrew Steele[12], and Kyle Uckert[2]

[1]Natural History Museum, London, UK, [2]NASA Jet Propulsion Laboratory, California Institute of Technology, Pasadena, CA, USA, [3]John Hopkins University, Baltimore, MD, USA, [4]NASA Johnson Space Center, Houston, TX, USA, [5]Photon Systems Inc., Covina, CA, USA, [6]INAF Osservatorio Astrofisico di Arcetri, Florence, Italy, [7]Amentum Jets II NASA Johnson Space Center, Houston, TX, USA, [8]Birkbeck University of London, London, UK, [9]Texas State University, San Marcos, TX, USA, [10]ARES NASA Johnson Space Center, Houston, TX, USA, [11]Planetary Science Institute, Tucson, AZ, USA, [12]Carnegie Institution for Science, Washington, DC, USA

Abstract The NASA Mars 2020 mission Perseverance rover carries a piece of Martian meteorite Sayh al Uhaymir (SaU) 008 as part of the calibration payload for the SHERLOC science instrument. We report SHERLOC observations of the SaU 008 flight piece over the first 1,000 sols of the mission and compare them to measurements done prior to launch, showing consistent detection of the same deep-ultraviolet (DUV) Raman and fluorescence signatures in the same locations. Co-located X-ray fluorescence (XRF) and DUV mapping of a reference SaU 008 piece on Earth confirm that the meteorite is comprised of an igneous mineral matrix consistent with shergottite, rich in olivine, maskelynite, and Fe-Mg pyroxenes detectable by SHERLOC. Terrestrial weathering features consist of fractures and vugs filled with Ca-carbonate. Fluorescence mapping reveals two major signatures: (a) broad-spectrum fluorescence present throughout the igneous matrix but strongest in weathering features, attributed to organic material, and (b) narrow-band 340 nm fluorescence spatially associated with ∼48 ppm cerium in <100 μm Ca-phosphate grains. Raman revealed organic material in both the igneous matrix and terrestrial carbonate in the form of macromolecular carbon (MMC) with defect and graphitic bands at ∼1,380 and ∼1,600 cm^{-1} respectively. Raman band parameters suggest that MMC associated with terrestrial weathering is less thermally mature, most likely the result of chemical alteration after landing on Earth. This study serves as a demonstration of SHERLOC's capabilities when supported by co-located XRF data from PIXL and suggests that SHERLOC can detect Ce in phosphate minerals at concentrations as low as 4 ppm.

Plain Language Summary The Perseverance rover of the NASA Mars 2020 mission carries a piece of Martian meteorite Sayh al Uhaymir (SaU) 008 as one of 10 calibration targets for the SHERLOC science instrument, providing ground truth testing of SHERLOC's ability to detect minerals and organic compounds on Mars. We report SHERLOC's observations of the SaU 008 target over the first 1,000 Martian days of the mission and compare them to measurements done on Earth, showing consistent detection of minerals and organics in the same locations. The meteorite itself consists of igneous rock with added carbonate from weathering after it landed on Earth. We observe two major fluorescence signatures: (a) a broad-band emission spectrum present throughout the meteorite's igneous rock, attributed to original Martian organic molecules, but strongest in weathered areas where organic molecules from Earth were introduced to the rock, and (b) a narrow-band 340 nm emission spectrum associated with 48 parts per million cerium in igneous phosphate grains. This study serves as a demonstration of SHERLOC's capabilities when supported by co-located XRF data from PIXL and suggests that SHERLOC may be able to detect cerium in phosphate minerals at concentrations as low as 4 parts per million.

1. Introduction

NASA's Perseverance rover landed on Mars in February 2021, and has since been exploring Jezero crater, the site of an ancient paleolake and river system from ∼3.5 billion years ago (Farley et al., 2022; Goudge et al., 2015, 2017, 2018; Horgan et al., 2020; Mangold et al., 2020, 2021; Schon et al., 2012; Stack et al., 2020). Two scientific

Resources: Marc Fries, Trevor Graff, Caroline Smith
Software: Joseph Razzell Hollis
Supervision: Rohit Bhartia, Kevin P. Hand
Validation: Joseph Razzell Hollis, Trevor Graff
Visualization: Joseph Razzell Hollis, Cindy Broderick, Yannick Buret
Writing – original draft: Joseph Razzell Hollis, Kelsey Moore
Writing – review & editing: Joseph Razzell Hollis, Kelsey Moore, Marc Fries, Cindy Broderick, Yannick Buret, Rohit Bhartia, Teresa Fornaro, Trevor Graff, Kevin P. Hand, Keyron Hickman-Lewis, Ryan Jakubek, Carina Lee, Francis M. McCubbin, Richard V. Morris, Ashley Murphy, Sunanda Sharma, Andrew Steele, Kyle Uckert

objectives of the mission are (a) characterize the geology of Mars, and (b) determine whether life ever existed on Mars (Farley et al., 2020; Williford et al., 2018). For this purpose, the Perseverance rover is equipped with several analytical instruments, including two spectrometers for mapping the organic and inorganic composition of rock samples at sub-millimeter resolution, named PIXL (Planetary Instrument for X-ray Lithochemistry) and SHERLOC (Scanning Habitable Environments with Raman and Luminescence for Organics and Chemicals) (Allwood et al., 2020; Bhartia et al., 2021). PIXL maps the spatial distribution of elements and their relative abundances with X-ray fluorescence (XRF), while SHERLOC maps the distribution of deep-ultraviolet (DUV) fluorescence emission and Raman scattering from both minerals and organic molecules. These techniques support one another in instances where detection of certain mineral phases is incomplete or impossible by one technique alone (Razzell Hollis et al., 2022; Scheller et al., 2022). While PIXL cannot directly detect organic material, the information it provides on host mineralogy and its elemental composition can be invaluable in interpreting data on organics from SHERLOC (Hickman-Lewis et al., 2022). For example, detection of a narrow-band DUV fluorescence signature at 340 nm, present in multiple targets on Mars, has spurred a line of questioning about whether SHERLOC is not just sensitive to organic luminescence but is also detecting inorganic luminescence from trace cerium in phosphate and perhaps sulfate grains on Mars (Scheller et al., 2022, 2024). To answer these questions and better define how SHERLOC and PIXL can be used to detect and study mixed inorganic/organic samples on Mars, we can turn to the martian meteorite SaU 008 as a case study of a martian rock studied on both Earth and Mars using PIXL and SHERLOC or their analog instruments.

SHERLOC possesses a set of 10 calibration targets (the SCT) that are mounted to the front of the rover chassis (Fries et al., 2022); one of these targets is a piece of martian meteorite named Sayh al Uhaymir (SaU) 008, the original parent sample of which was found in Oman in 1999. SaU 008 is one of several shergottitic martian meteorites that are known to contain a mix of igneous minerals and original martian organic material at ppm levels, as well as evidence of chemical alteration and contamination from terrestrial weathering after their arrival on Earth (O'Brien & Clare, 2022; Steele et al., 2016). It was included on the SCT for scientific outreach and to provide a representative martian sample of known composition that can be used to provide in situ confirmation of SHERLOC's ability to detect organic and inorganic signatures in martian rocks during the mission (Fries et al., 2022). This target (henceforth referred to as the "flight" piece) was characterized in detail prior to launch using the SHERLOC laboratory prototype instrument, named MOBIUS (mineralogy and organic based investigations with ultraviolet spectroscopy), and has been scanned 9 times by SHERLOC over the first 1,000 sols after landing on Mars. By analyzing SHERLOC observations of the flight piece of SaU 008 over the first 1,000 sols of the mission and comparing those measurements to terrestrial observations of both the flight piece before launch and of reference SaU 008 pieces that were retained on Earth, we can directly assess the effectiveness of SHERLOC at detecting known organic and inorganic signatures in a definitively Mars-relevant rock.

1.1. Background: Martian Meteorites

SaU 008 is one of ten paired martian meteorites found in the same area of Oman since 1999 and is the largest of the ten at 8.58 kg across two fragments (Grossman, 2000; Walton et al., 2005). Mineralogical analysis of SaU 005, 008, and 150, among others, has established that these meteorites are geochemically depleted olivine-phyric shergottites consisting of large (~3 mm) olivine crystals in a fine-grained pyroxene/plagioclase groundmass that is principally pigeonite and maskelynite with minor augite, chromite, and merrillite (Goodrich, 2003; Zipfel, 2000). The martian origin of these meteorites is confirmed by bulk composition and isotope analysis, and the presence of maskelynite and shock melt pockets (9%–11% by volume) within the meteorite bodies suggests that they experienced impact shock pressures of 33–45 GPa (Walton et al., 2005). Olivine-phyric shergottites have characteristically low abundances of light rare earth elements (Udry et al., 2020), and bulk analysis of SaU 005 reports that it contains an average of <0.6 parts per million (ppm) Cerium (Dreibus et al., 2000). Like other meteorites found in hot deserts, SaU 005 and 008 are reported to have terrestrial weathering features—specifically evaporitic calcium carbonate that forms a crust on exposed surfaces and partially fills fractures and voids within the meteorite body (Crozaz & Wadhwa, 2001; Dreibus et al., 2000). Other martian meteorites from separate falls are known to have similar compositions, including Dar al Gani 476/489/735/670/876/975 (Zipfel, 2000).

Shergottitic meteorites like SaU 008 typically contain ~18 ± 26 ppm total reduced carbon (Steele et al., 2016), primarily in the form of macromolecular carbon (MMC), also known as carbonaceous matter, consisting of cross-linked assemblages of different organic molecules usually rich in polyaromatic units resulting from gradual graphitization and maturation of the MMC by thermal metamorphism (Steele, McCubbin, Fries, Golden,

et al., 2012, 2016). Martian meteorites can contain both original organic material from Mars and organic material introduced by terrestrial weathering after their arrival on Earth. Original martian organics occur as highly mature, high temperature carbon that was initially referred to by Wright et al., and Grady et al., as igneous carbon but later shown to be present within mineral inclusions of the igneous matrix (Wright et al., 1986; Grady et al., 2004; Steele, McCubbin, Fries, Golden, et al., 2012, Steele, McCubbin, Fries, Kater et al., 2012), while organics in weathering features are less mature, lower temperature and exhibit a distinct isotopic composition typical of terrestrial organic material (Barrat et al., 1998; Lee et al., 2017; Toporski & Steele, 2007). The organic component of SaU 008 is readily detectable to Raman spectroscopy via the defective (D) and graphitic (G) bands of MMC at 1,380 and ∼1,600 cm^{-1} respectively (Fries et al., 2022; Steele, McCubbin, Fries, Golden, et al., 2012), and the properties of such bands can be invaluable for assessing the thermal maturity of MMCs (Ferrari & Robertson, 2000; Henry et al., 2019; Quirico et al., 2009, 2020; Steele et al., 2016).

2. Methods

2.1. Sample Curation and Preparation

All three pieces of SaU 008 used in this study were cut and processed at the Meteorite Thin Section Laboratory at the NASA Johnson Space Center (JSC) using the method described by Fries et al. (2022). The "flight" piece is a cylindrical wafer that was integrated into the SHERLOC calibration target palette and sent to Mars onboard Perseverance; the "reference" piece is an irregularly shaped slice that was stored at NASA Jet Propulsion Laboratory (JPL), USA, for future reference and analysis; the "NHM" piece (SaU 008-A, P31346) is one of three rectangular slices that were returned to the meteorites collection at the Natural History Museum in London, UK, to be kept as witness samples. Cutting was done using a Buehler Isomet saw with a diamond blade, exposed surfaces gently lapped and then cleaned in an ultrasonic bath containing pure ethanol. Reference and NHM samples were wrapped in clean aluminum foil and stored in air-conditioned rooms.

2.2. Terrestrial XRF Spectroscopy

XRF mapping was done on a Bruker M4 Tornado microXRF at the California Institute for Technology. All maps and elemental quantifications were obtained at 2 mbar pressure to improve the quantification of light elements. However, even under these conditions, light elements including C and Na were not detected and quantified. Normalization of data from likely carbonate regions was calculated assuming the presence of C. Data were collected using two silicon drift detectors with no primary beam filters. The X-ray tube voltage was 50 kV and current was 400 μA with detectors set to measure 90 keV and 130 kcps. Mapping was conducted with a spot size of 20 μm. Upon completion of mapping, regions of interest (ROIs) were selected based on elemental maps to target specific minerals of interest for elemental quantification. Elemental abundances for ROIs were quantified using Bruker M4 Tornado software. These compositions are spatial averages due to both the XRF spot size and ROI area and therefore likely reflect some mixing of phases. Still, quantifications provide useful insight into the compositions of the ROIs that allow for the identification of mineral phases based on consistency with known mineral compositions. The combination of elemental mapping and quantification provided a map of interpreted mineral distributions which could be spatially correlated with Raman and fluorescence data.

2.3. Terrestrial DUV Spectroscopy

DUV Raman and fluorescence spectral mapping of both the flight piece (pre-launch) and reference piece were done on MOBIUS, the laboratory prototype for SHERLOC at NASA JPL. MOBIUS uses a 248.579 nm NeCu pulsed laser (Photon Systems, Inc.) reflected off a 248 nm RazorEdge ultra-steep long-pass edge filter (Semrock, Inc.) and focused onto the sample through a chromatically corrected *f*/4 objective lens (ThorLabs LMU-5x-UVB). The focused laser spot is a 40 μm diameter Gaussian-blurred ellipse, as described by Razzell Hollis et al. (2020). Raman scattering and fluorescence emissions were collected in a 180° back-scattering geometry using a Horiba 550i spectrometer with a slit width of 250 mm and recorded by a Horiba Symphony e2v 42-10 CCD liquid nitrogen-cooled (−140°C) detector. Fluorescence measurements were performed using a 300 lines/mm grating with a spectral range of 250–410 nm and a spectral binning of 0.16 nm, while Raman measurements were performed using an 1,800 lines/mm grating with a spectral range of 800–4,200 cm^{-1} and a spectral binning of 3.8 cm^{-1} per pixel. Spectral maps were acquired by taking a spectrum at each point in a grid, with a varying number of points and point-to-point step size depending on desired coverage and spatial resolution (Table 1).

Table 1
Summary of MOBIUS and SHERLOC Scans Taken for Each Piece of SaU 008 as of June 2024

Sample	MOBIUS scan	MOBIUS mode	Pulses per point (ppp)	Dimensions (mm)	Step size (μm)
Flight	F-F1	Fluor.	25	22.6 × 22.0	500
	F-F2	Fluor.	25	5.4 × 1.8	100
	F-F3	Fluor.	25	8.3 × 7.8	100
	F-F4	Fluor.	25	5.6 × 2.3	50
	F-R2	Raman	1,200	5.4 × 1.8	100
	F-R4	Raman	1,200	5.5 × 2.2	100
Reference	S-F1 (Area 1)	Fluor.	25	4.8 × 2.5	50
	S-F2 (Area 2)	Fluor.	25	4.8 × 2.0	50
	S-F3 (Area 3)	Fluor.	25	4.8 × 2.5	50
	S-F4 (Survey)	Fluor.	25	14.4 × 11.7	100
	S-R1 (Area 1)	Raman	1,200	4.8 × 2.5	100
	S-R2 (Area 2)	Raman	1,200	4.8 × 2.0	100
	S-R3 (Area 3)	Raman	1,200	4.8 × 2.5	100
Sample	SHERLOC scan	SHERLOC mode	Pulses per point (ppp)	Dimensions (mm)	Step size (μm)
Flight	Sol 59	Survey	10	7.0 × 7.0	200
	Sol 181	Survey	15	5.0 × 5.0	140
	Sol 181	HDR	300	7.0 × 7.0	780
	Sol 368	Detail	500	1.0 × 1.0	100
	Sol 545	Detail	500	1.0 × 1.0	100
	Sol 704	Detail	500	1.0 × 1.0	100
	Sol 712	Survey	15	5.0 × 5.0	140
	Sol 712	Detail	900	1.0 × 1.0	100
	Sol 935	Detail	500	1.0 × 1.0	100

Note. MOBIUS operates in two modes: Fluorescence only and Raman only. SHERLOC has three typical scan settings, acquiring Raman and fluorescence simultaneously and differing only in terms of area, resolution, and laser pulses used: Survey = fewer pulses, large area, high spatial resolution; HDR = High Dynamic Range, more pulses, large area, low spatial resolution; Detail = even more pulses, small area, highest spatial resolution.

Raman and fluorescence measurements were taken using 1,200 and 25 laser pulses per point (ppp), respectively, at 40 pulses per second with a pulse width of 40 μs and a typical pulse energy of 2–3 μJ. A total of 4 fluorescence maps and 2 Raman maps were taken of the flight piece (Fries et al., 2022), and 4 fluorescence maps and 3 Raman maps of the reference piece (Table 1). Terrestrial DUV spectra were pre-processed to correct for laser output variation and remove any cosmic rays (Uckert et al., 2019). Further data processing (spectral recalibration, baseline subtraction, peak detection, and spectral map visualization) was performed by custom Python scripts utilizing NumPy (Harris et al., 2020), SciPy (van de Walt et al., 2014; Virtanen et al., 2020), and LMFIT (Newville et al., 2014) packages. Raman shift values were recalibrated using a linear correction derived from regular measurements of acetonitrile standard with 4 major peaks between 919 and 2,942 cm^{-1} (254.37–268.17 nm). Raman spectra were baselined using polynomials fitted to areas of low signal. Raman and fluorescence intensity maps were generated by summing the intensity of each spectrum in 3 specified spectral regions and assigning the intensities to the R, G, B values of the corresponding pixel, normalized to the 2nd and 98th percentiles for all three bands across the entire map. Mineralogical ROIs were identified using XRF and defined by circles with diameter 0.4 mm (0.2 mm for phosphate), averaging all spectra within each circle. Fitting of the organic D and G band region (900–1,800 cm^{-1}) was adapted from the model described by Kouketsu et al. (2014) using a pseudo-Voigt (PV) function to represent each of the G (~1,600 cm^{-1}) and D1–4 modes (~1,375, ~1,670, ~1,275, ~1,470 cm^{-1}). Three additional PV functions were included for material peaks at 1,010 cm^{-1} (silicate), 1,080 cm^{-1} (carbonate), and 1,175 cm^{-1} (unassigned), and a symmetric Fermi-Dirac (FD) function with a fixed position and width (determined from fitting of blank spectra) was included to account for the known Raman peak

of atmospheric O_2 at 1,556 cm^{-1}. PV functions in the fit were allowed to vary in position by ±30 cm^{-1} with an upper FWHM limit of 100 cm^{-1}. All Python scripts used for data processing are available online (Razzell Hollis, 2024).

2.4. SHERLOC Spectroscopy

The flight piece was also mapped using SHERLOC after landing on Mars on sols 59, 181, 368, 704, 712, and 935 (as of June 2024). Like MOBIUS, SHERLOC uses a pulsed NeCu laser (248.579 nm) but has a ∼110 μm diameter elliptical laser spot at focus (Bhartia et al., 2021). SHERLOC collects Raman and fluorescence spectra simultaneously with a spectral range of 250–355 nm (∼300–12000 cm^{-1}) and a spectral bin size of ∼0.1 nm (∼10 cm^{-1}) in the Raman region (Uckert et al., 2021). Survey maps were done using 36 × 36 points, 10–15 pulses per point (ppp), high dynamic range (HDR) maps were 10 × 10 points at 250–300 ppp, and detail maps were 10 × 10 points, 500–900 ppp. SHERLOC spectra are read out in three separate CCD regions to limit the contribution of dark noise on binned pixels and are recombined during processing to recreate the full spectrum. For Raman-specific analyses, only region 1 (∼250–275 nm, ∼200–4,000 cm^{-1}) is used to reduce the cumulative effect of dark noise from other detector regions on weak features (Bhartia et al., 2021). Spectral calibration was performed prior to launch using acetonitrile, highly oriented pyrolytic graphite (HOPG), Hg lamp emission lines, and calcite standards, and refined after landing using internal and external calibration targets (Fries et al., 2022; Uckert et al., 2021). Initial data processing was performed using publicly available Loupe software for dark frame subtraction, laser normalization, and cosmic ray removal (Uckert, 2022). Further data processing was done using custom Python scripts using the same methods for terrestrial DUV spectroscopy as described above. SHERLOC measurements of the flight piece are described in Table 1 and the scanned areas are illustrated in Figure 1. Visible light images of the external calibration target on Mars were taken using SHERLOC's internal Autofocus Context Imager (ACI) camera and the Wide-Angle Topographic Sensor for Operations and eNgineering (WATSON) camera (Wogsland et al., 2023). All Python scripts used for data processing are available online (Razzell Hollis, 2024).

2.5. Trace Elemental Analysis

Mineralogy and trace element analysis of the NHM piece was done at the Natural History Museum in London, UK, using a TIMA Scanning Electron Microscope (SEM) followed by a laser ablation inductively coupled plasma mass spectrometer (LA-ICP-MS). The TIMA instrument was equipped with four EDAX Element 30 Energy Dispersive X-ray Spectroscopy (EDS) detectors and was operated at 25 kV accelerating voltage, 13–14 nA probe current and a working distance of 15 mm. Analysis of the polished 25 mm block acquired over 18 million EDS points over a duration of 5.5 hr. Mineralogy was determined by collecting Back Scattered Electron mapping (BSE) combined with EDS analysis at 3 μm pixel resolution with a total of 1000 X-ray counts per pixel. LA-ICP-MS trace element mapping of a 1 × 1 mm area was carried out using a Teledyne Iridia 193 nm laser ablation system coupled to an Agilent 8900 ICP-MS using the Aerosol Rapid Introduction System (ARIS). A spot size of 3 μm and repetition rate of 357 Hz were used. Isotopes measured were ^{24}Mg (2 ms), ^{27}Al (2 ms), ^{43}Ca (4 ms), ^{88}Sr (2 ms), ^{89}Y (2 ms), and ^{140}Ce (4 ms). Laser mapping conditions were optimized using the QuadLock (Norris et al., 2021). Element maps were quantified using HDIP v.1.8. The maps were segmented using the Labeled Segments tool in HDIP to isolate the phosphate grains. NIST610 glass was used as the calibration reference material and the Ca concentration of stoichiometric merrillite ($Ca_9MgNa(PO_4)_7$; 34.36 wt.%) was used as the internal standard.

3. Results and Discussion

A total of 3 samples of SaU 008 were analyzed in this study: the flight piece onboard Mars 2020, the reference piece stored at NASA JPL, and the NHM piece stored at the NHM. Comparison of optical images and maps from DUV Raman, XRF, and SEM-EDS presented in this article demonstrate that while SaU 008 is a heterogenous sample containing lots of different grains of varying sizes, the 3 samples analyzed in this paper are compositionally similar, reflecting their origins as close cuttings from the same rock.

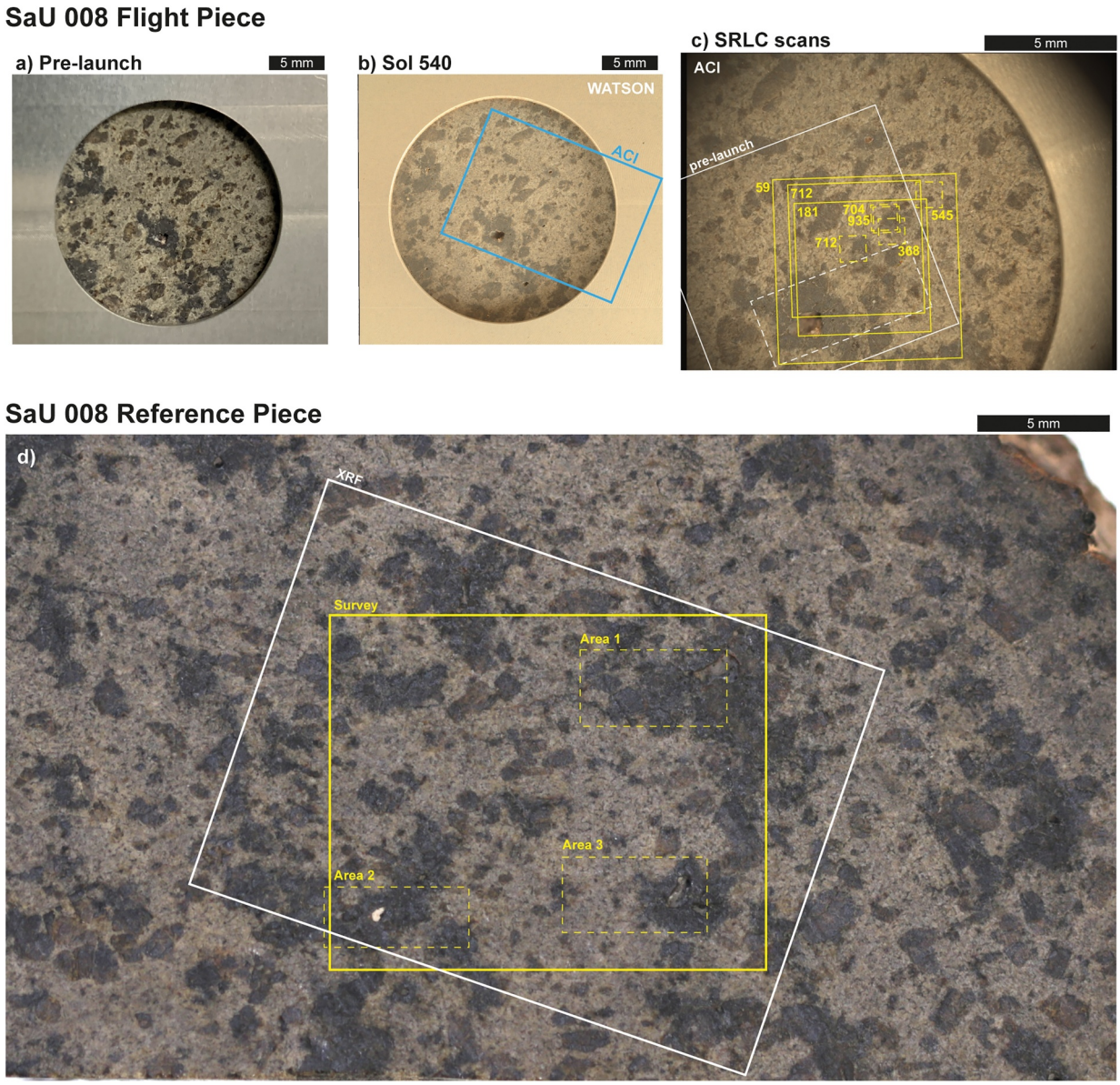

Figure 1. (a) Photograph of the Sayh al Uhaymir (SaU) 008 meteorite calibration target (the flight piece) taken during pre-launch characterization. (b) WATSON image of the flight piece taken on sol 540 of the mission on Mars. (c) The meteorite calibration target as seen by the SHERLOC autofocus context imager (ACI) on sol 545, colorized and illustrated to show footprints of the pre-launch MOBIUS maps (white) and SHERLOC maps (yellow) as of sol 935. (d) Photograph of the SaU 008 reference piece, illustrated to show footprints of X-ray fluorescence (white), DUV fluorescence (solid yellow), and DUV Raman (dashed yellow) maps.

3.1. Mineral Detections

The visible matrix of the SaU 008 reference piece consists of light and dark toned regions composed primarily of mafic silicate and aluminosilicate minerals, readily identifiable by their elemental compositions as quantified by XRF (Table 2), that include olivine, plagioclase, and pyroxenes. XRF mapping (Figure 2) shows that the composition of light-toned regions is consistent with a mix of small plagioclase feldspar and larger Mg-rich pyroxenes, while dark-toned regions include large, relatively Fe-rich grains that are compositionally consistent with olivine (Fo62-74) phenocrysts and areas consistent with pyroxene/plagioclase glasses. Based on previous reports on this and paired meteorites, the plagioclase fraction takes the form of the shocked amorphous phase maskelynite, produced during impact shock pressures of 33–45 GPa (Ali et al., 2018; Walton et al., 2005). Shock-induced heating has also produced visible melt pocket regions and glasses (Figure 2). The meteorite has also been extensively modified by terrestrial weathering after landing on Earth, with voids and fracture lines that crosscut

Table 2
XRF Elemental Quantifications (in Normalized wt%) for Key Igneous Matrix Minerals and Secondary Minerals

Oxide	Bulk	Olivine	Maskelynite	Pyroxene	Carbonate	Phosphate
Na_2O	0.46	0.00	0.00	0.00	0.00	0.41
MgO	18.51	31.36	1.07	22.70	7.24	9.48
Al_2O_3	7.17	0.28	24.61	1.39	2.34	4.93
SiO_2	44.71	32.56	52.56	47.84	15.00	33.33
P_2O_5	0.40	0.02	0.00	0.03	0.26	11.93
SO_3	0.35	0.02	0.11	0.06	0.70	2.32
K_2O	0.06	0.01	0.03	0.00	0.35	0.02
CaO	5.57	0.38	11.30	3.81	59.22	13.74
TiO_2	0.41	0.03	0.21	0.37	0.16	1.89
MnO	0.79	0.12	0.55	1.39	1.35	0.70
Cr_2O_3	0.79	0.12	0.55	1.39	1.35	0.70
Fe_2O_3	20.97	34.66	9.35	21.84	12.92	20.78
NiO	0.04	0.03	0.00	0.01	0.04	0.13
ZnO	0.01	0.01	0.00	0.01	0.04	0.01
SrO	0.01	0.00	0.00	0.01	0.05	0.00

Note. Each quantification is averaged from at least 3 locations in Areas 1–3 indicated in Figure 3. Values may not add up to 100 wt% due to instrumental error.

the meteorite body and are very rich in Ca compared to the surrounding igneous matrix. This Ca-rich phase may be carbonate, but as XRF alone cannot directly detect carbon, the presence of carbonate can only be inferred from anomalously low wt% totals relative to other regions that indicate that a significant component of the material is not accounted for. The complex mineralogy revealed by XRF is consistent with previous reports on this and paired meteorites that describe them as olivine-phyric shergottites consisting of olivine, pyroxene, and shocked maskelynite, with in-filled fractures and other weathering features rich in calcite (Dreibus et al., 2000; Goodrich, 2003).

DUV Raman spectroscopy is also capable of detecting a number of different minerals in SaU 008, as the average Raman spectra in Figure 3 show. These spectra were averaged over several ROI identified with each type of mineral. Both maskelynite and pyroxene exhibit a single Raman peak at 1,000–1,020 cm^{-1}, attributed to a Si–O stretching mode common to both (Razzell Hollis et al., 2021; Shkolyar et al., 2021). Plagioclases and pyroxenes are usually distinguished from one another using Si–O–Si bending and tetrahedral modes at <850 cm^{-1}, however we are unable to detect these in the MOBIUS data because the MOBIUS instrument's edge filter significantly attenuated all signals below 800 cm^{-1}. Olivine is similarly difficult to detect, though for other reasons: the diagnostic olivine doublet at 820 and 850 cm^{-1} (Kuebler et al., 2006) is not readily observed in the MOBIUS data, which may be attributable to the local enrichment of Fe in the Fo62-74 olivine phase. Octahedral Fe^{2+} ions have strong absorption bands in the UV range, which will attenuate both the incident 248.6 nm laser as it passes through the sample and any Raman scattering produced (Razzell Hollis et al., 2020, 2021). Separate measurements of terrestrial olivine standards show that the MOBIUS instrument can detect a single convolved peak at ~825 cm^{-1} for low-Fe olivines (Fo# 80–90, see Supporting Information S1), but more Fe-rich olivines are less likely to produce a detectable level of Raman scattering. The threshold will depend on the instrument and acquisition parameters used: SHERLOC's sensitivity in this spectral region may be sufficiently high enough to detect the Fo62-74 olivine peak at ~825 cm^{-1} in SaU 008 and at ~830 cm^{-1} in other igneous rocks on the Martian surface (Razzell Hollis et al., 2022). Areas identified as melt pockets (glass) exhibited a weaker, broader silicate peak compared to other igneous mineral ROIs, likely due to structural disorder in the amorphous silicate glass. The challenges associated with detecting and distinguishing Fe-rich silicate minerals solely using DUV spectroscopy highlight the importance of conducting co-located DUV and XRF measurements to conclusively confirm mineralogy by combining Raman detections with elemental compositions.

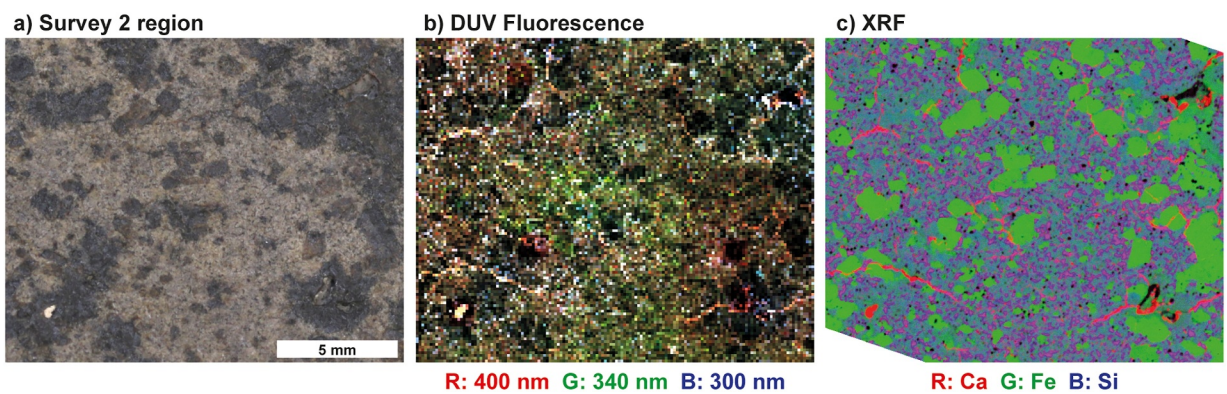

Figure 2. Large area maps of the survey region of the Sayh al Uhaymir 008 reference piece showing the visible image (a), DUV fluorescence intensity (b) measured by the MOBIUS instrument (scan S-F4), and elemental composition measured by X-ray fluorescence (XRF) (c). See Supporting Information S1 for individual maps of fluorescence intensity at each wavelength and XRF maps of each element.

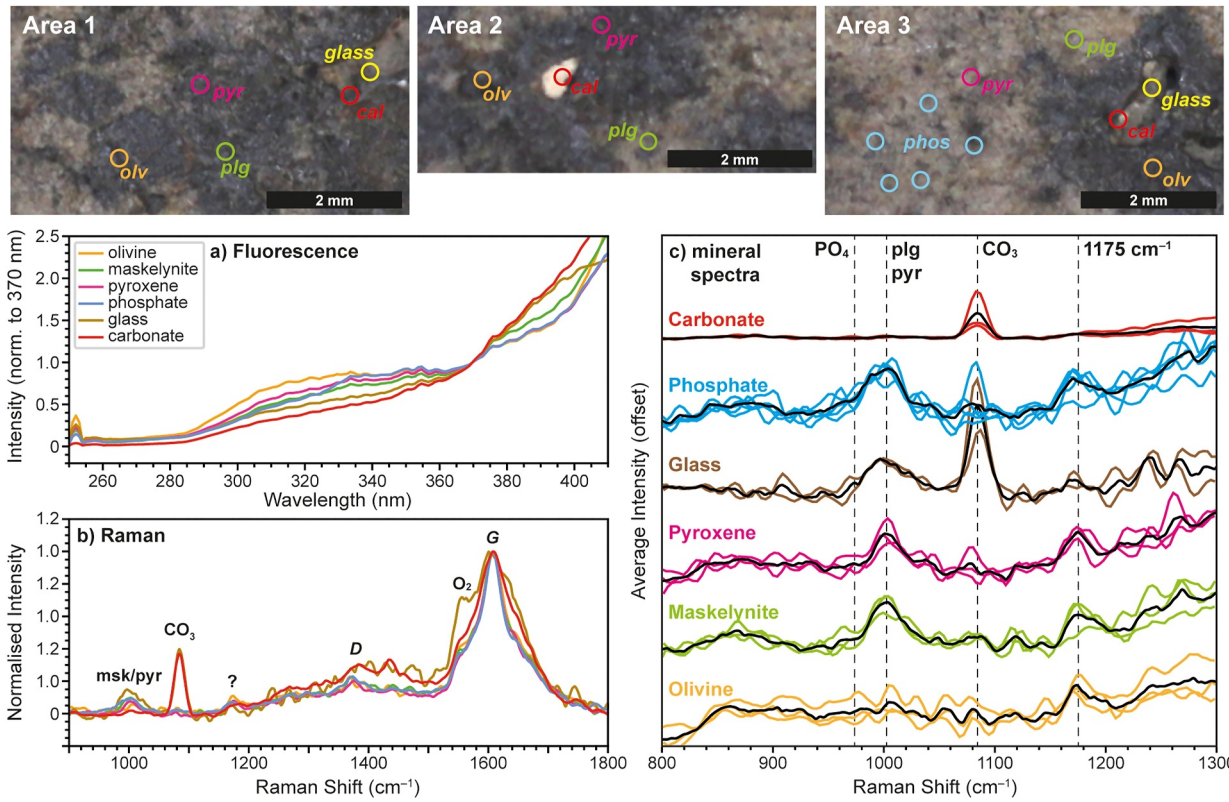

Figure 3. Average DUV Fluorescence (a) and Raman (b) spectra for different mineral phases in the reference piece as measured by MOBIUS (scans S-F1 to S-F3, S-R1 to S-R3). Each spectrum was averaged over all regions of interest (ROIs) indicated for that mineral, shown by open circles with diameter 0.4 mm. Key: olv = olivine, msk = maskelynite, pyr = pyroxene, phos = phosphate, cal = calcite. Raman peak assignments as follows: sil. = silicate, CO_3 = carbonate, D = defective organic carbon band, G = graphitic organic carbon band, O_2 = atmospheric oxygen, ? = unassigned 1,175 cm^{-1} mode. (c) variation in mineral peaks between ROIs, black lines indicate the average spectra for all ROIs of each mineral. Fluorescence spectra were normalized at 370 nm.

The igneous matrix also contains many small (~100 μm) phosphate grains identified by local enrichment of P, though their small size and estimated composition ~8 wt% P_2O_5 suggests the XRF spot incorporates substantial signal from the surrounding silicate matrix. A relatively high Ca content (9.2% CaO) suggests that the P-bearing phase is primarily a calcium-bearing phosphate such as apatite or merrillite. Ca phosphates are among the most common phosphates found in martian meteorites, including shergottites, and they are typically in the form of merrillite and apatite (Hausrath et al., 2024; McCubbin et al., 2016; Shearer et al., 2015). This could be confirmed by DUV Raman based on the position of the v_1 peak of $[PO_4]^{3-}$ ion at 975 cm^{-1}, but even when spectra from 5 phosphate grains were averaged together, we could not confidently identify any peaks around 960–975 cm^{-1} (Figure 3c). However, given the size of the phosphate grains is comparable to the MOBIUS laser spot size (40 μm) and the scan step size (100 μm), there is a chance we missed the phosphate grain entirely and, like XRF, the relative overlap of the laser spot and irregularly shaped phosphate grains may mean even a perfectly targeted single point spectrum may end up interrogating the surrounding mineral matrix more than the grain itself (see Supporting Information S1).

In addition to igneous silicate minerals, DUV Raman spectroscopy is also able to detect secondary minerals from terrestrial weathering of the meteorite after it landed on Earth, specifically carbonate deposited along a series of narrow fracture lines and voids throughout SaU 008. The presence of carbonate in these regions is identified by a strong Raman peak at 1,080 cm^{-1}, assigned to the v_1 stretching mode of the $[CO_3]^{2-}$ ion. The observed peak position is consistent with calcium carbonate, specifically calcite (Razzell Hollis et al., 2022), and this identification is confirmed by co-located XRF detection of Ca enrichment and low total %wt abundances in the same areas (Figure 4). Carbonate was also detected in glassy regions, and based on the spatial distribution of 1,080 cm^{-1} signal and Ca enrichment, it appears that glassy regions are rimmed in calcite. The combined use of DUV Raman spectroscopy and XRF mapping provides a more detailed characterization of chemistry and

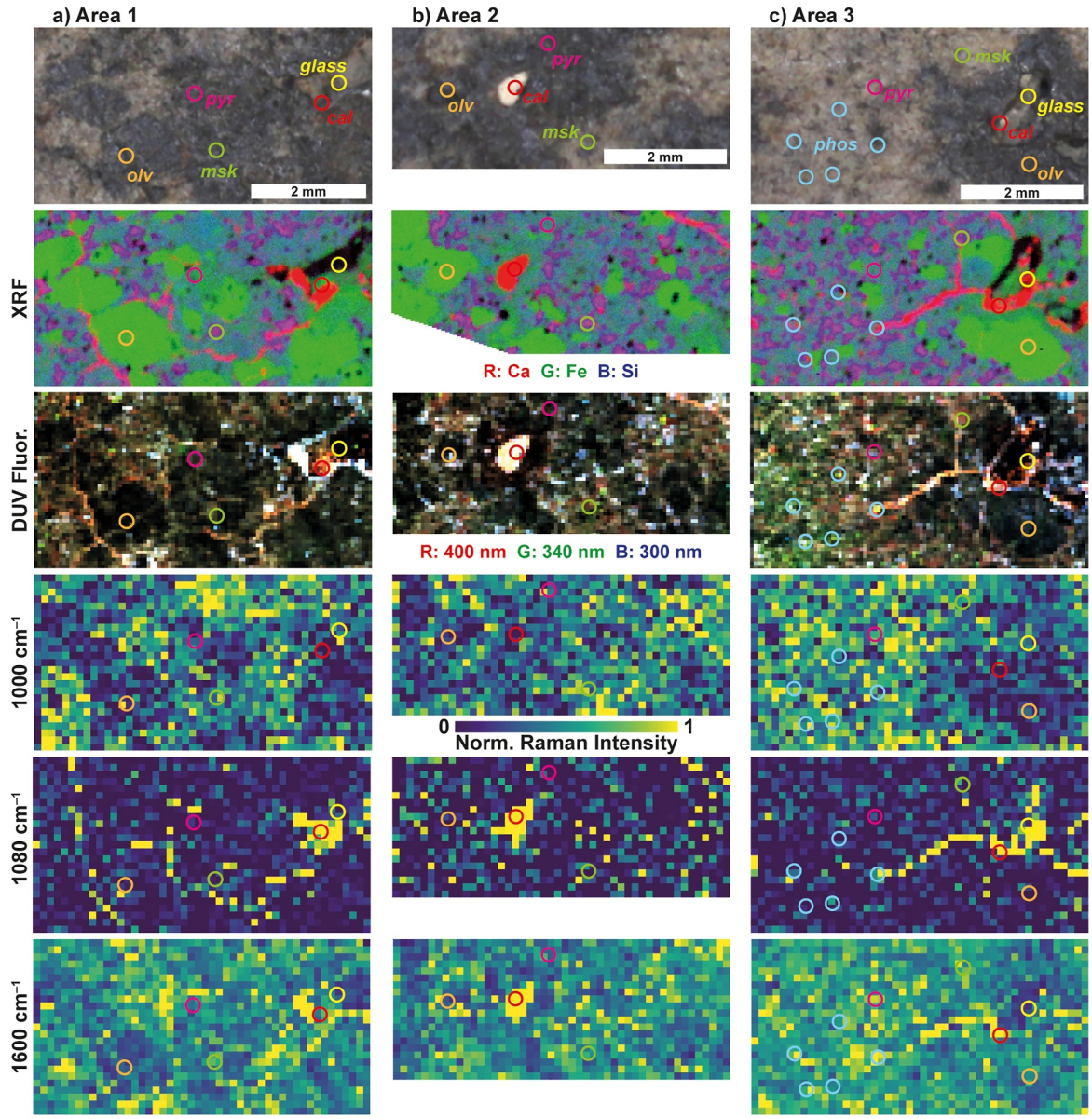

Figure 4. Local high-resolution X-ray fluorescence elemental maps and DUV Raman and Fluorescence maps for Areas 1 (a), 2 (b), and 3 (c) of the reference piece of Sayh al Uhaymir 008. DUV fluorescence maps show the distribution of intensity at 400, 350, and 300 nm as red, green, and blue, respectively. Raman maps illustrate the spatial distribution of intensity at 1,000 cm^{-1} (silicate), 1,080 cm^{-1} (carbonate) and 1,600 cm^{-1} (organics). Representative grains of key mineral phases are highlighted by colored circles in each map labeled as follows: olv = olivine, msk = maskelynite, pyr = pyroxene, phos = phosphate, cal = carbonate.

mineralogy than either technique could achieve alone (Razzell Hollis et al., 2022). While the MOBIUS and SHERLOC instruments cannot readily distinguish pyroxene and maskelynite using only the ~1,000 cm^{-1}, these phases have distinctly different elemental compositions that are easily distinguished by XRF, and while the calcite present weathering features is only detectable by XRF as a local enrichment of Ca and low total abundances, Raman instruments can directly detect the carbonate ion by its peak at ~1,080 cm^{-1}. This demonstrates that co-located mapping of martian targets with both SHERLOC and PIXL on Mars has and will continue to provide the best chance for Perseverance to interrogate both igneous and alteration mineralogy in situ.

As well as identifiable mineral peaks, Figure 3b also indicates the presence of a peak at 1,175 cm^{-1} that could not be assigned to a specific material, although it is present in several different ROIs. Spectral intensity maps (see Supporting Information S1) suggest that this peak is distributed unevenly across the meteorite, and correlation analysis of fitted peak intensities suggests that the 1,175 cm^{-1} peak is slightly more correlated to organic peaks

than to inorganic peaks, with an average Pearson correlation coefficient of ∼0.41 versus ∼0.28 respectively (see Supporting Information S1). It is possible that this is the dominant scattering mode of a surface contaminant introduced during polishing/cleaning of the cut meteorite. No other unattributed peaks were observed between 850 and 4,000 cm^{-1}.

3.2. Organic Content of SaU 008

SaU 008 and other igneous martian meteorites are reported to contain reduced organic carbon at around 18 ppm by weight, after discounting potential terrestrial contamination (Steele, McCubbin, Fries, Kater, et al., 2012, 2016). The organic carbon is readily detectable to DUV spectroscopy by both its broad fluorescence signature (with a maximum >410 nm, shown as yellow-orange in the false color maps of Figures 2–4) and the Raman D and G bands of macromolecular carbon (MMC). The corresponding spectra are shown in Figure 3. Comparison of the spatial distribution of MMC, silicate, and carbonate intensities (Figure 4) suggests that the MMC component is (a) present throughout the igneous mineral matrix, and (b) particularly concentrated in areas containing carbonates from terrestrial weathering, such as fracture lines and the vug in Area 2. The D and G bands are not specific to any one organic molecule but represent a weighted average of the entire continuum of different polyaromatic units present within MMC. Under visible excitation, most MMC exhibits a strong well-defined D band but under DUV excitation, the G band dominates due to resonant enhancement of scattering from highly graphitized polyaromatic units within MMC (Quirico et al., 2020). Strong resonance is also responsible for the detection of a second order G band overtone at ∼3,220 cm^{-1}, that is, at roughly twice the fundamental frequency (see Supporting Information S1).

The parameters of the D and G bands can be used to indirectly measure the structural properties or geothermal history of both terrestrial and extraterrestrial MMCs (Ferrari & Robertson, 2000), but many different models and methods have been described for conducting this type of analysis. Most models require deconvoluting the D and G bands with between two and five functions of varying type to represent overlapping modes, and for DUV spectra acquired on MOBIUS, we found the most appropriate model is a five-function (G, D1, D2, D3, D4) Lorentzian–Gaussian model adapted from (Kouketsu et al., 2014), with additional functions to account for observed peaks from other materials (Figure 5). When the D and G bands observed in each mineralogical ROI were fitted using this model, we found that the igneous matrix ROIs (olivine, maskelynite, pyroxene, phosphate) contain very similar MMC in terms of their Raman parameters: a G band function centered at 1,605–1,607 cm^{-1} with a full-width-half-maximum (FWHM, or Γ_G) of 55–65 cm^{-1}, and a D1/G peak intensity ratio (known as parameter R1) of 0.17–0.21. For the glass and carbonate ROIs associated with terrestrial weathering, Γ_G increased to 93–94 cm^{-1} and R1 increased to 0.20–0.27 (Table 3). This suggests that organic material within the igneous matrix is more thermally mature, while organic material within weathering features is less mature, consistent with previous studies on paired stones and other martian meteorites that report that highly reduced, high-temperature carbon originally from Mars exist within mineral inclusions of the igneous matrix (Grady et al., 2004; Jull et al., 2000; Lee et al., 2017; Steele, McCubbin, Fries, Golden, et al., 2012, Steele, McCubbin, Fries, Kater et al., 2012; Wright et al., 1986), while the terrestrial weathering features contain low-temperature, possibly biological, carbon contaminants introduced after arrival on Earth (Barrat et al., 1998; Becker et al., 1999; Lee et al., 2017; O'Brien & Clare, 2022; Steele et al., 2016; Toporski & Steele, 2007). The distribution of low-maturity organic material within carbonate-filled fractures and other shock features is also consistent with previous reports (Becker et al., 1999; Steele et al., 2016). Contamination can include organics directly introduced from the terrestrial environment or through chemical alteration of the original martian MMC during terrestrial weathering.

When fitted parameters are compared to observed trends for terrestrial MMCs of varying thermal maturity (48 coal standards from lignite to anthracite), we find that the igneous MMC falls near the thermally mature end of the terrestrial MMC trend, but the weathered MMC does not line up well with any part of the trend (Figure 5). This agrees with other studies that have reported significant discrepancies for meteoritic MMC versus terrestrial MMC in terms of both composition and the structural changes that result from increasing maturity (Bower et al., 2013; Derenne & Robert, 2010; O'Brien & Clare, 2022; Steele et al., 2016). Further investigation is needed to determine what is responsible for the discrepancy in D and G parameters for extraordinary samples such as meteorites, as most interpretations of D and G band properties are done in the context of terrestrial systems, where the bands are diagenetic features associated with the maturation of biological material. In samples such as Martian meteorites and carbonaceous chondrites, the initial MMC chemical composition is not biogenic in nature and has been shown

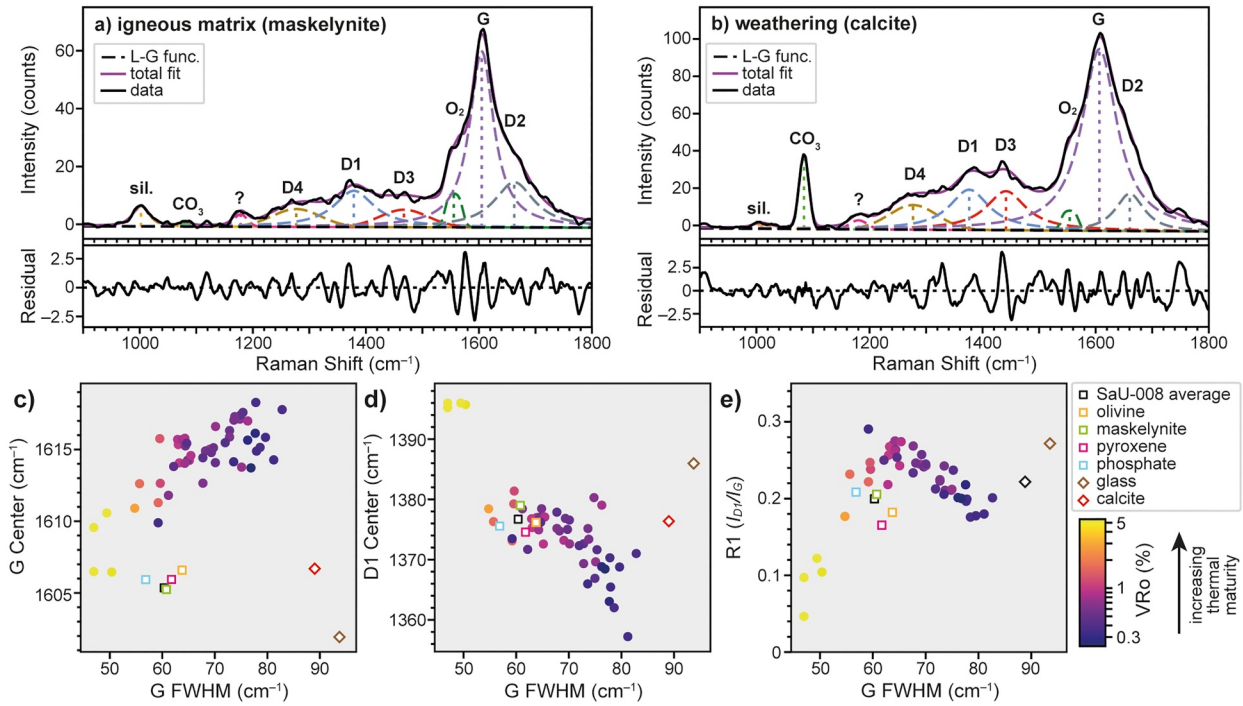

Figure 5. Deconvolution of the average DUV Raman spectrum for (a) maskelynite and (b) carbonate regions of interest (ROIs) using a linear combination of mixed Lorentzian–Gaussian (L–G) (pseudo-Voigt) functions, with the residual of each fit shown beneath. (c–e) Key D and G band parameters from fitting of each Sayh al Uhaymir 008 ROI (squares: igneous, diamonds: weathering) versus fitted parameters for 48 terrestrial coal standards (circles) with varying thermal maturity from lignite to anthracite, colored by their vitrinite reflectance (VRo). ROI spectra derived from MOBIUS scans S-R1 to S-R3.

to be reliant on the starting material and possible aqueous/thermal metamorphism (Busemann et al., 2009; Cody et al., 2011; Steele, McCubbin, Fries, Golden, et al., 2012). Consequently, typical terrestrial trends in D and G band parameters may not apply to all forms of MMC and interpretation of these parameters in the context of extraterrestrial carbon sources must be done carefully and cautiously (Pasteris & Wopenka, 2003). As a result, we are currently unable to estimate any metamorphic temperatures from the DUV Raman spectra of meteoritic MMCs. Despite this limitation, we show that not only can instruments like SHERLOC directly detect MMC within martian rock but also can qualitatively distinguish between different types of organic material and, with support from PIXL, begin to interpret organic origin and history in the context of different host minerals.

3.3. DUV Fluorescence Signatures

Under 248 nm excitation, the reference piece exhibits two major DUV fluorescence signatures: (a) a broad-band fluorescence with a maximum at more than 410 nm, and (b) a narrower fluorescence with a maximum intensity at ~340 nm. The first is the semi-ubiquitous signature that appears green-yellow-orange in the false-color maps of Figures 2–4. This signature is seen in both igneous matrix regions and terrestrial weathering features and is typified by having an onset at 280 nm and rising in intensity toward a maximum beyond the MOBIUS instrument's spectral range (>410 nm, see Figure 3a). It is weaker in dark-toned regions, stronger in light-toned regions, and strongest along carbonate-filled fracture lines and in bright vug features like the one in Area 2 (Figure 4). We attribute this broad-band fluorescence to organic material, specifically MMC, based on spatial correlation to the Raman D and G bands (Figure 4). A fluorescence maximum at >410 nm suggests that most of the fluorescence emission comes from aromatic units containing 3 or more fused rings, as monocyclic and bicyclic aromatic molecules tend to have fluorescence maxima between 270 and 400 nm (Razzell Hollis et al., 2023).

The second fluorescence signature, with a maximum at 340 nm, is much less common but occurs in very small (<200 μm) hot-spots in the igneous matrix, appearing blue-white in the false-color maps of Figures 2–4. It is most obvious in igneous mineral ROIs spectra, but even then it does not occur in isolation, appearing on top of the broad-band organic fluorescence (Figure 3a). A similar fluorescence signature with a maximum at ~340 nm has

Table 3
Fitted D and G Parameters for Average Raman Spectra by Mineralogical ROI

Region	ω_G (cm^{-1})	Γ_G (cm^{-1})	ω_D (cm^{-1})	Γ_D (cm^{-1})	R1	RA1
Average	1,606	60	1,377	100	0.20	0.44
Olivine	1,607	64	1,376	100	0.18	0.45
Maskelynite	1,605	61	1,379	100	0.21	0.44
Pyroxene	1,606	62	1,375	77	0.17	0.45
Phosphate	1,606	57	1,376	96	0.21	0.43
Glass	1,602	94	1,386	100	0.27	0.44
Carbonate	1,607	89	1,376	100	0.20	0.44

Note. Fitting was done using a 5-function Lorentzian–Gaussian model. ω = peak center, Γ = peak full-width-half-maximum, R1 = D1/G intensity ratio, RA1 = (D1 + D4)/(D1 + D2 + D3 + D4 + G) integrated intensity ratio. ROI spectra derived from MOBIUS scans S-R1 to S-R3.

been repeatedly observed in Martian rocks by SHERLOC and has been tentatively assigned to inorganic fluorescence emission by Ce^{3+}-bearing phosphate grains based on co-located detection of phosphate by PIXL on Mars (Scheller et al., 2022, 2024; Sharma et al., 2023). Previous reports on the composition of SaU 005 (a paired stone) indicate that these meteorites contain ~1 ppm Ce by bulk weight, but Ce and other REEs are known to be concentrated in late-stage crystallization phases like phosphates (Dreibus et al., 2000). Comparison of 340 nm fluorescence and P content distribution in the SaU 008 reference piece (Figure 6a) confirms that 340 nm emission is highly localized, occurring in regions <100 μm in diameter that are associated with Ca-phosphate grains, such as ROIs 3 and 4 in Figure 6a. Areas of high fluorescence that have little P content, such as ROI 5, exhibit only the broad-band fluorescence signature with no narrow-band 340 nm signature apparent on top of it.

To establish whether the 340 nm fluorescence is actually due to trace Ce present in the phosphate phase, we conducted BSE-EDS and LA-ICP-MS measurements of another sample of SaU 008, the NHM piece. BSE-EDS measurements confirm that the phosphate grains are highly irregular, <100 μm grains of merrillite ($Ca_9NaMg(PO_4)_7$, shown in pink in Figure 4b) embedded in the igneous matrix, consistent with the reports of phosphate minerals present in SaU 005 (Ward et al., 2017). The Ce concentration of the phosphate ROIs in the reference piece was too low to be detected by XRF (see Supporting Information S1), but subsequent LAI-ICP-MS measurements of the NHM piece confirm that phosphate grains in the meteorite are significantly enriched in Ce relative to the surrounding silicate matrix, with an average Ce concentration of 48 ppm by weight. This is similar to the 46 ± 4 ppm Ce reported by Ward et al. (2017) for merrillite grains in SaU 005. Consequently, we conclude that the narrow-band 340 nm fluorescence signature associated with igneous Ca-phosphate grains in SaU 008 is due to trace Ce^{3+} present in the phosphate phase, and that DUV fluorescence instruments like SHERLOC are very

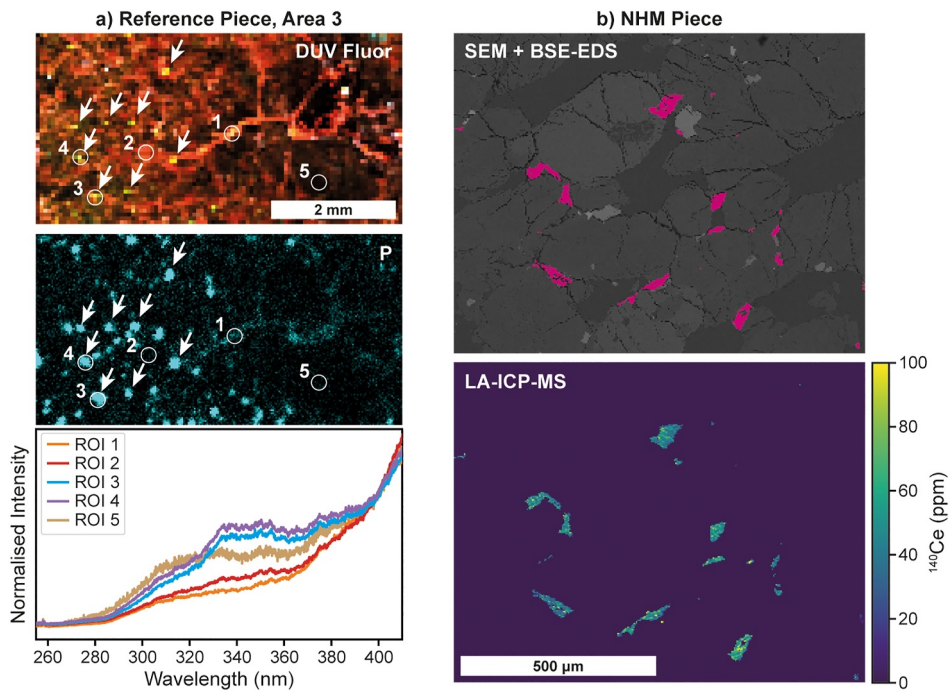

Figure 6. (a) DUV fluorescence map versus P intensity from X-ray fluorescence of Area 3 on the reference piece of Sayh al Uhaymir 008 (scan S-F3). Arrows point to phosphate grains that are co-located with 340 nm fluorescence. Open circles indicate phosphate and non-phosphate regions of interest (0.2 mm diameter) with corresponding average DUV fluorescence normalized to intensity at 400 nm. (b) SEM image of NHM piece overlaid with phosphate grain regions identified by BSE-EDS; LA-ICP-MS map of the same area, showing Ce-140 concentration in parts per million.

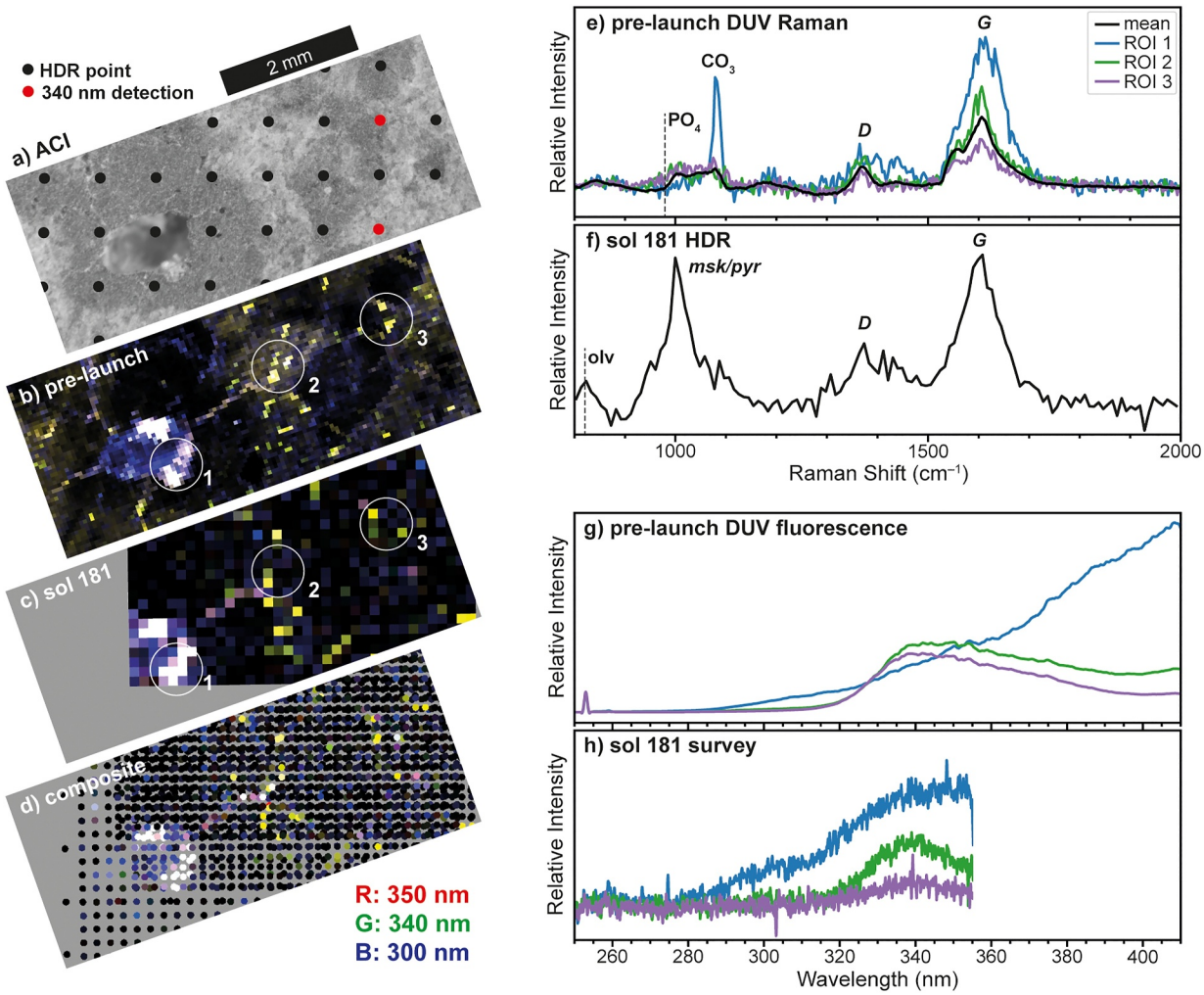

Figure 7. (a) SHERLOC ACI image of the mapped region of the flight piece, highlighting points measured by SHERLOC in the sol 181 HDR (500 ppp, 780 μm steps). (b) pre-launch fluorescence map (scan F-F4, 25 ppp, 50 μm steps), with regions of interest (ROIs) marked. (c) subsection of the SHERLOC sol 181 survey (15 ppp, 100 μm steps), with the same ROIs. (d) Composite of all SHERLOC fluorescence maps of this area, each point measurement indicated by a 100 μm diameter circle. (e) Mean pre-launch Raman spectra for each ROI, with major Raman peak assignments. (f) Mean SHERLOC Raman spectrum for the meteorite target, HDR scan on sol 181. (g) Mean pre-launch fluorescence spectra for each ROI. (h) Mean SHERLOC fluorescence spectra for each ROI, survey scan on sol 181.

sensitive to the presence of Ce. Given that Ce^{3+} fluorescence occurs at wavelengths associated with 2–3 ring aromatic organics, care must be taken when interpreting fluorescence signatures lest Ce fluorescence be mistaken as evidence of organics (Shkolyar et al., 2021). For conclusive organic detection using DUV spectroscopy, fluorescence signatures should be distinct from known inorganic emission signatures and should be corroborated by co-located observations of unambiguous organic Raman signatures such as the D and G bands of MMC. Elemental analysis by XRF, particularly in terms of known REE-supporting phases like phosphates, can further support interpretation of fluorescence signatures.

3.4. SHERLOC Observations of SaU 008 on Mars

The SaU 008 flight piece was characterized by the MOBIUS instrument prior to launch in order to provide a co-located reference data set for direct comparison to SHERLOC measurements acquired during the mission (Figure 7). Pre-launch characterization of the flight piece included DUV Raman and fluorescence maps with resolutions as high as 50 μm, measured on the MOBIUS instrument. The pre-launch fluorescence map (Figure 7) shows the same signatures seen in the reference piece, first the broad-band organic fluorescence signature with an onset around 280 nm and a maximum at more than 400 nm (depicted as blue-white in Figure 7), and second, the narrow band Ce^{3+}-in-phosphate fluorescence signature with an onset at 320 nm and a maximum at 340 nm

(depicted as yellow in Figure 7). The organic signature, like in the reference piece, is strongest around a hollow vug rich in carbonate (ROI #1) and along several narrow fracture lines, consistent with pre-launch DUV measurements of the flight piece. The Ce^{3+}-in-phosphate fluorescence signature occurs only in very small hotspots (100–200 μm in size, highlighted in ROIs #2–3) within the igneous matrix, consistent with the size of phosphate grains observed by XRF in the reference piece and by BSE-EDS in the NHM piece.

Since landing on Mars, the SHERLOC instrument has conducted 9 scans of the flight piece, and as was first reported by Fries et al. (2022), it is readily capable of detecting fluorescence signals from SaU 008 even with short exposures of just 15 laser pulses per point (∼120 μJ at start of mission). The fluorescence survey scan taken on sol 181 overlaps much of the area shown in Figure 7b and clearly reproduces the spatial distribution of fluorescence signal, albeit at lower spatial resolution (Figure 7c). SHERLOC observes the same broad-band fluorescence signature rising toward longer wavelengths that we associate with organic material in the carbonate-rich vug region (ROI #1 in Figure 7h), and the Ce^{3+}-in-phosphate signature is apparent in ROIs #2–3 as a narrow band with a maximum at 340 nm. The different spatial distributions of these signatures are also readily distinguishable, with the organic signature appearing strongest in weathering features, such as the vug and fracture lines, whereas the inorganic Ce signature occurs as single point detections due to the phosphate grain size (∼100 μm) being comparable to or smaller than the SHERLOC laser spot diameter (∼110 μm) and the step size (∼140 μm for the sol 181 survey shown in Figure 7c). When all SHERLOC scans of the area in Figure 7a are plotted together (Figure 7d), accounting for the SHERLOC spot size of ∼100 μm, they provide a more accurate reproduction of the spatial distribution of fluorescence signal seen in the pre-launch map, allowing individual phosphate grains to be identified. The overall fluorescence of the meteorite in terms of spectra and spatial distribution observed prior to launch is well reproduced in subsequent SHERLOC maps, suggesting that there has been little change in the composition or distribution of fluorescent material between the spacecraft leaving Earth in July 2020 and landing on Mars in February 2021. SHERLOC generally exhibits lower signal and greater noise than laboratory instruments used for pre-launch measurements, attributed to a warmer detector (SHERLOC operates around −28°C vs. MOBIUS at −140°C) and a higher incidence of cosmic ray interference on Mars.

The detection of the Ce^{3+}-in-phosphate fluorescence signal at 340 nm by SHERLOC also provides us a measure of how sensitive SHERLOC is to the presence of trace Ce. SHERLOC obtained 900 counts of fluorescence intensity using an exposure time of 15 laser pulses. Assuming this was achieved by the best possible overlap between the annular laser spot and a typical larger (∼100 μm length) phosphate grain containing 48 ppm Ce, we get an estimated sensitivity of 1.25 counts per input μJ per ppm Ce (see Supporting Information S1 for calculation). Then, if the minimum signal noise ratio (SNR) required for confident detection is 10:1, a 15 ppp survey can detect Ce at concentrations as low as ∼32 ppm Ce. For longer exposures (e.g., 500–900 ppp) used in HDR or Detail scans, SHERLOC's limit of detection may be as low as 4 ppm Ce. Consequently, it appears that DUV fluorescence spectroscopy is exceptionally sensitive to Ce fluorescence, and care must be taken to distinguish inorganic from organic fluorescence when searching for potential organic biosignatures in rocks on Mars (Shkolyar et al., 2021).

Using longer exposures (300 ppp and higher), SHERLOC can detect Raman features associated with both the igneous silicate matrix and the organic component of SaU 008. Individual ROI spectra are not shown as the HDR scan did not have a high enough point density to capture all three ROIs, and so only the 100-point scan average is shown in Figure 7f. As with pre-launch measurements, SHERLOC detects maskelynite and pyroxene but cannot differentiate them based on the ∼1,000 cm^{-1} peak alone. SHERLOC also detects the Fo62-74 olivine phase, the olivine doublet appearing as a single convolved peak at 825 cm^{-1}, but assignment of this peak to olivine is complicated by a known SHERLOC instrumental feature at ∼820 cm^{-1} from the fused silica optics used. If it is olivine, it appears to be convolved due to SHERLOC's relatively large spectral resolution, ∼40 cm^{-1} in the Raman region (Bhartia et al., 2021). The intensity ratio of the olivine doublet is known to reflect Fo# (Kuebler et al., 2006), and that information may still be indicated by the position of the convolved olivine peak (Jakubek et al., 2023).

SHERLOC also detects the D and G bands of organic material at 1,380–1,400 and 1,605–1,610 cm^{-1}, which are on average comparable to the same bands measured before launch by MOBIUS, exhibiting similar band properties consistent with a high level of thermal maturity and an overall SNR of 87:1. The only meaningful change from pre-launch spectra is that the overall Raman intensity of MMC is much lower relative to the silicate peak at ∼1,000 cm^{-1}, with the G/silicate intensity ratio decreasing from 10:1 prior to launch to 1.2:1 on sol 181. This may

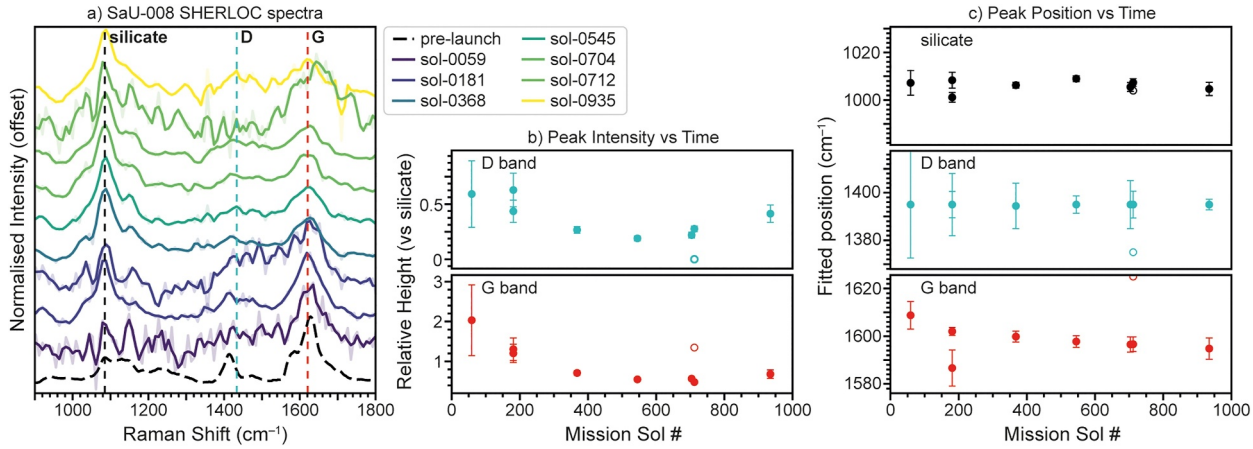

Figure 8. Variation in Sayh al Uhaymir 008 spectra over time on Mars as measured by SHERLOC. (a) Smoothed average spectra for each scan versus the pre-launch spectrum acquired on MOBIUS (averaged over F-R2 to F-R4). (b) Fitted Raman intensities for D and G bands over time, relative to silicate peak at ~1,000 cm^{-1}. (c) Fitted peak positions for each peak over time. Open circles indicate results from spectra where standard errors could not be calculated from fitting.

be due to differences in instrumental sensitivity between MOBIUS and SHERLOC, or a consequence of surface sampling given that the spectrum shown in Figure 7f is an average of just 100 point measurements across a 5 × 5 mm area—if none of the points coincide with an organic-rich weathering feature, then the average spectrum will only be representative of the relatively organic-poor igneous silicate matrix, whereas the pre-launch maps always included organic-rich carbonate-filled features that would raise the average organic/silicate intensity ratio. The larger spectral resolution of SHERLOC versus laboratory instruments, ~40 cm^{-1} versus ~25 cm^{-1}, appears to have little effect on already broad peaks such as the silicate and organic bands, but care should still be taken when comparing SHERLOC spectra to laboratory instrument data, especially for narrower mineral peaks that will be more sensitive to spectral resolution (Bhartia et al., 2021; Jakubek et al., 2023).

When the average spectra for each of the 9 scans are plotted against one another (Figure 8), it confirms that the flight piece of SaU 008 continues to exhibit a ~1,000 cm^{-1} silicate peak from maskelynite/pyroxene even after 1,000 sols on the surface of Mars. However, the intensity of the organic G band declined over time on Mars, relative to the silicate peak, decreasing from 1.2 ± 0.2 on sol 181 to 0.68 ± 0.11 on sol 935, and the G band position also shifted slightly, from 1,602 ± 1.7 cm^{-1} on sol 181 to 1,595 ± 4.5 cm^{-1} on sol 935. The G band FWHM could not be reliably assessed due to low SNR in later scans. The observed changes in the organic component of the meteorite may be the result of radiation-induced degradation of MMC over time on the surface of Mars: the calibration target is oriented vertically, facing forwards relative to the rover, but is otherwise still exposed to ambient irradiation. However, it is difficult to tell whether the decline in signal is the result of a genuine loss of organic material over time, increasing attenuation of the G band by the accumulation of Fe-rich silicate dust on the calibration target, or simply because each observation of the target is measuring the organic content of a slightly different area (as shown in Figure 1). Given the dimensions of the carbonate-filled weathering features, with fracture lines less than half the width of the SHERLOC laser spot, even small variations in point location between scans could result in completely different material being illuminated (Razzell Hollis et al., 2022), leading to large changes in apparent intensity between maps that ostensibly overlap. Determining whether the variation is due to sampling or actual degradation of material under ambient martian conditions could be done by repeatedly scanning the same area of SaU 008, using the laser to remove dust, and/or systematic laboratory studies to observe how dramatically location sampling can influence observed organic/silicate ratio variance.

4. Conclusions

Using combined XRF and DUV Raman/Fluorescence spectroscopy of martian meteorite SaU 008, we were able to assess its igneous and alteration mineralogy, detect and characterize organic material in terms of macromolecular carbon (MMC), and determine the spatial distribution of organics within a complex mineral matrix. By assessing the reference piece in detail, we are able to connect and correlate observations of the flight piece made

by SHERLOC on Mars and assess its ability to detect and identify both mineralogy and organic content in rocks of martian provenance.

Based on the results described above, we have demonstrated that the Perseverance rover's scientific payload can conduct detailed analysis of the mineralogy and organic composition of target rocks on Mars. We show that SHERLOC is able to detect both inorganic Ce^{3+} fluorescence and organic fluorescence signatures at extremely low concentrations in SaU 008, with an estimated limit of detection of ~4 ppm Ce^{3+} within phosphate grains. Detection of organics on Mars from their Raman scattering is more elusive, but SaU 008 shows it is possible and can be invaluable even if only D and G bands are identified, enabling qualitative assessment of thermal maturity through fitting of band parameters, which can be used to distinguish original martian MMC and terrestrial contamination in SaU-008. For quantitative measurement of metamorphic temperatures from organic Raman spectra, further work is needed to better establish the trends exhibited by terrestrial MMC standards (e.g., coals) under DUV excitation with similar instrumentation, and to assess the effects of alteration/degradation on observed Raman signatures. Case studies such as SaU 008 are invaluable for understanding the spectra we obtain on Mars, and in identifying targets of high scientific value that merit sampling for a potential return to Earth at a future date.

Data Availability Statement

All DUV spectra acquired using the MOBIUS instrument are archived on the SHERLOC Open Data Repository and are free to use with appropriate acknowledgments (Razzell Hollis et al., 2024). SHERLOC data of the SaU 008 flight piece on Mars are available on the NASA Planetary Data System and are free for public use (Beegle & Bhartia, 2020). The SHERLOC and WATSON images shown in Figure 1 are available on the NASA Raw Images portal via https://mars.nasa.gov/mars2020/multimedia/raw-images/ and are free for public use. The following images were used:

WATSON image of SaU 008 calibration target on sol 540:

- SIF_0540_0714896818_941FDR_N0263008SRLC07024_0000LMJ01

SHERLOC ACI image of calibration target on sol 545:

- SC3_0545_0715349045_300ECM_N0265150SRLC15032_0000LMJ01_SI1_0540_0714896818_941ECM_N0263008SRLC07024_0000LMJ01

Acknowledgments
This effort was carried out in part at the Jet Propulsion Laboratory, California Institute of Technology, under a contract with the National Aeronautics and Space Administration (80NM0018D0004). XRF measurements were performed with support from Caltech GPS Division Analytical Facility and the Simons Foundation. This work was funded in part by a NASA Postdoctoral Program fellowship awarded to Joseph Razzell Hollis, administered by the Universities Space Research Association on behalf of NASA. This work was supported in part by the ISFM Mission Enabling Work Package at the Johnson Space Center. Teresa Fornaro was supported by ASI/INAF agreement no. 2023-3-HH, Mini Grant Ricerca Fondamentale INAF 2022.

References

Ali, A., Jabeen, I., Nasir, S., & Banerjee, N. (2018). Oxygen isotope thermometry of DaG 476 and SaU 008 Martian meteorites: Implications for their origin. *Geosciences*, *8*(1), 15. https://doi.org/10.3390/geosciences8010015

Allwood, A. C., Wade, L. A., Foote, M. C., Elam, W. T., Hurowitz, J. A., Battel, S., et al. (2020). Pixl: Planetary instrument for X-Ray lithochemistry. *Space Science Reviews*, *216*(8), 134. https://doi.org/10.1007/s11214-020-00767-7

Barrat, J. A., Gillet, P., Lécuyer, C., Sheppard, S. M. F., & Lesourd, M. (1998). Formation of carbonates in the tatahouine meteorite. *Science*, *280*(5362), 412–414. https://doi.org/10.1126/science.280.5362.412

Becker, L., Popp, B., Rust, T., & Bada, J. L. (1999). The origin of organic matter in the Martian meteorite ALH84001. *Advances in Space Research*, *24*(4), 477–488. https://doi.org/10.1016/S0273-1177(99)00090-3

Beegle, L. W., & Bhartia, R. (2020). Mars 2020 perseverance rover SHERLOC raw, partially processed, and derived data products [Dataset]. *Mars 2020 Perseverance Rover SHERLOC Raw, Partially Processed, and Derived Data Products*. https://doi.org/10.17189/1522643

Bhartia, R., Beegle, L. W., Deflores, L., Abbey, W., Razzell Hollis, J., Uckert, H., et al. (2021). Perseverance's scanning habitable environments with raman and luminescence for organics and chemicals (SHERLOC) investigation. *Space Science Reviews*, *217*(4), 58. https://doi.org/10.1007/s11214-021-00812-z

Bower, D. M., Steele, A., Fries, M. D., & Kater, L. (2013). Micro Raman spectroscopy of carbonaceous material in microfossils and meteorites: Improving a method for life detection. *Astrobiology*, *13*(1), 103–113. https://doi.org/10.1089/ast.2012.0865

Busemann, H., Nguyen, A. N., Cody, G. D., Hoppe, P., Kilcoyne, A. L. D., Stroud, R. M., et al. (2009). Ultra-primitive interplanetary dust particles from the comet 26P/Grigg–Skjellerup dust stream collection. *Earth and Planetary Science Letters*, *288*(1–2), 44–57. https://doi.org/10.1016/j.epsl.2009.09.007

Cody, G. D., Heying, E., Alexander, C. M. O., Nittler, L. R., Kilcoyne, A. L. D., Sandford, S. A., & Stroud, R. M. (2011). Establishing a molecular relationship between chondritic and cometary organic solids. *Proceedings of the National Academy of Sciences*, *108*(48), 19171–19176. https://doi.org/10.1073/pnas.1015913108

Crozaz, G., & Wadhwa, M. (2001). The terrestrial alteration of Saharan shergottites Dar al Gani 476 and 489: A case study of weathering in a hot desert environment. *Geochimica et Cosmochimica Acta*, *65*(6), 971–977. https://doi.org/10.1016/S0016-7037(00)00586-X

Derenne, S., & Robert, F. (2010). Model of molecular structure of the insoluble organic matter isolated from murchison meteorite: Model of molecular structure of murchison IOM. *Meteoritics & Planetary Sciences*, *45*(9), 1461–1475. https://doi.org/10.1111/j.1945-5100.2010.01122.x

Dreibus, G., Spettel, B., Haubold, R., Jochum, K. P., Palme, H., Wolfe, D., & Zipfel, J. (2000). Chemistry of a new shergottite: Sayh al uhaymir 005. *Meteoritics & Planetary Sciences*, *35*(5), A49.

Farley, K. A., Stack, K. M., Shuster, D. L., Horgan, B. H. N., Hurowitz, J. A., Tarnas, J. D., et al. (2022). Aqueously altered igneous rocks sampled on the floor of jezero crater, Mars. *Science*, *377*(6614), eabo2196. https://doi.org/10.1126/science.abo2196

Farley, K. A., Williford, K. H., Stack, K. M., Bhartia, R., Chen, A., de la Torre, M., et al. (2020). Mars 2020 mission overview. *Space Science Reviews*, *216*(8), 142. https://doi.org/10.1007/s11214-020-00762-y

Ferrari, A. C., & Robertson, J. (2000). Interpretation of Raman spectra of disordered and amorphous carbon. *Physical Review B*, *61*(20), 14095–14107. https://doi.org/10.1103/physrevb.61.14095

Fries, M. D., Lee, C., Bhartia, R., Razzell Hollis, J., Beegle, L. W., Uckert, K., et al. (2022). The SHERLOC calibration target on the Mars 2020 perseverance rover: Design, operations, outreach, and future human exploration functions. *Space Science Reviews*, *218*(6), 46. https://doi.org/10.1007/s11214-022-00907-1

Goodrich, C. A. (2003). Petrogenesis of olivine-phyric shergottites Sayh al Uhaymir 005 and elephant moraine A79001 lithology A. *Geochimica et Cosmochimica Acta*, *67*(19), 3735–3772. https://doi.org/10.1016/S0016-7037(03)00171-6

Goudge, T. A., Milliken, R. E., Head, J. W., Mustard, J. F., & Fassett, C. I. (2017). Sedimentological evidence for a deltaic origin of the western fan deposit in Jezero crater, Mars and implications for future exploration. *Earth and Planetary Science Letters*, *458*, 357–365. https://doi.org/10.1016/j.epsl.2016.10.056

Goudge, T. A., Mohrig, D., Cardenas, B. T., Hughes, C. M., & Fassett, C. I. (2018). Stratigraphy and paleohydrology of delta channel deposits, Jezero crater, Mars. *Icarus*, *301*, 58–75. https://doi.org/10.1016/j.icarus.2017.09.034

Goudge, T. A., Mustard, J. F., Head, J. W., Fassett, C. I., & Wiseman, S. M. (2015). Assessing the mineralogy of the watershed and fan deposits of the Jezero crater paleolake system, Mars. *Journal of Geophysical Research: Planets*, *120*(4), 775–808. https://doi.org/10.1002/2014JE004782

Grady, M. M., Verchovsky, A. B., & Wright, I. P. (2004). Magmatic carbon in Martian meteorites: Attempts to constrain the carbon cycle on Mars. *International Journal of Astrobiology*, *3*(2), 117–124. https://doi.org/10.1017/S1473550404002071

Grossman, J. N. (2000). The meteoritical bulletin, no. 84, 2000 August. *Meteoritics & Planetary Sciences*, *35*(S5), A199–A225. https://doi.org/10.1111/j.1945-5100.2000.tb01797.x

Harris, C. R., Millman, K. J., Van Der Walt, S. J., Gommers, R., Virtanen, P., Cournapeau, D., et al. (2020). Array programming with NumPy. *Nature*, *585*(7825), 357–362. https://doi.org/10.1038/s41586-020-2649-2

Hausrath, E. M., Adcock, C. T., Berger, J. A., Cycil, L. M., Kizovski, T. V., McCubbin, F. M., et al. (2024). Phosphates on Mars and their importance as igneous, aqueous, and astrobiological indicators. *Minerals*, *14*(6), 591. https://doi.org/10.3390/min14060591

Henry, D. G., Jarvis, I., Gillmore, G., & Stephenson, M. (2019). Earth-science reviews Raman spectroscopy as a tool to determine the thermal maturity of organic matter: Application to sedimentary, metamorphic and structural geology. *Earth-Science Reviews*, *198*, 102936. https://doi.org/10.1016/j.earscirev.2019.102936

Hickman-Lewis, K., Moore, K. R., Hollis, J. J., Tuite, M. L., Beegle, L. W., Bhartia, R., et al. (2022). In situ identification of Paleoarchean biosignatures using colocated perseverance rover analyses: Perspectives for in situ Mars science and sample return. *Astrobiology*, *22*(9), 1143–1163. https://doi.org/10.1089/ast.2022.0018

Horgan, B. H. N., Anderson, R. B., Dromart, G., Amador, E. S., & Rice, M. S. (2020). The mineral diversity of Jezero crater: Evidence for possible lacustrine carbonates on Mars. *Icarus*, *339*, 113526. https://doi.org/10.1016/j.icarus.2019.113526

Jakubek, R. S., Bhartia, R., Uckert, K., Asher, S. A., Czaja, A. D., Fries, M. D., et al. (2023). Calibration of Raman bandwidths on the scanning habitable environments with raman and luminescence for organics and chemicals (SHERLOC) deep ultraviolet raman and fluorescence instrument aboard the perseverance rover. *Applied Spectroscopy*, *78*(9), 993–1008. https://doi.org/10.1177/00037028231210885

Jull, A. J. T., Beck, J. W., & Burr, G. S. (2000). Isotopic evidence for extraterrestrial organic material in the Martian meteorite, Nakhla. *Geochimica et Cosmochimica Acta*, *64*(21), 3763–3772. https://doi.org/10.1016/S0016-7037(00)00458-0

Kouketsu, Y., Mizukami, T., Mori, H., Endo, S., Aoya, M., Hara, H., et al. (2014). A new approach to develop the Raman carbonaceous material geothermometer for low-grade metamorphism using peak width. *Island Arc*, *23*(1), 33–50. https://doi.org/10.1111/iar.12057

Kuebler, K. E., Jolliff, B. L., Wang, A., & Haskin, L. A. (2006). Extracting olivine (Fo-Fa) compositions from Raman spectral peak positions. *Geochimica et Cosmochimica Acta*, *70*(24), 6201–6222. https://doi.org/10.1016/j.gca.2006.07.035

Lee, N. N., Fritz, J., Fries, M. D., Gil, J. F., Beck, A., Pellinen-Wannberg, A., et al. (2017). The extreme biology of meteorites: Their role in understanding the origin and distribution of life on Earth and in the universe. In H. Stan-Lotter & S. Fendrihan (Eds.), *Adaption of microbial life to environmental extremes* (pp. 283–325). Springer International Publishing. https://doi.org/10.1007/978-3-319-48327-6_11

Mangold, N., Dromart, G., Ansan, V., Salese, F., Kleinhans, M. G., Massé, M., et al. (2020). Fluvial regimes, morphometry, and Age of jezero Crater Paleolake inlet Valleys and their exobiological significance for the 2020 rover Mission landing site. https://doi.org/10.1089/ast.2019.2132

Mangold, N., Gupta, S., Gasnault, O., Dromart, G., Tarnas, J. D., Sholes, S. F., et al. (2021). Perseverance rover reveals an ancient Delta-Lake system and flood deposits at Jezero crater, Mars. *Science*, *374*(6568), 711–717. https://doi.org/10.1126/science.abl4051

McCubbin, F. M., Boyce, J. W., Srinivasan, P., Santos, A. R., Elardo, S. M., Filiberto, J., et al. (2016). Heterogeneous distribution of H 2 O in the Martian interior: Implications for the abundance of H 2 O in depleted and enriched mantle sources. *Meteoritics & Planetary Sciences*, *51*(11), 2036–2060. https://doi.org/10.1111/maps.12639

Newville, M., Stensitzki, T., Allen, D. B., & Ingargiola, A. (2014). Lmfit: Non-linear least-square minimization and curve-fitting for python. *Zenodo*. Retrieved from https://zenodo.org/record/11813

Norris, C. A., Danushevsky, L., Olin, P., & West, N. R. (2021). Elimination of aliasing in LA-ICP-MS by alignment of laser and mass spectrometer. *Journal of Analytical Atomic Spectrometry*, *36*(4), 733–739. https://doi.org/10.1039/D0JA00488J

O'Brien, & Clare, Á. (2022). Extra-terrestrial organics: Organic matter in meteorites and Martian analogues. https://doi.org/10.5525/GLA.THESIS.83255

Pasteris, J. D., & Wopenka, B. (2003). Necessary, but not sufficient: Raman identification of disordered carbon as a signature of ancient life. *Astrobiology*, *3*(4), 727–738. https://doi.org/10.1089/153110703322736051

Quirico, E., Bonal, L., Montagnac, G., Beck, P., & Reynard, B. (2020). New insights into the structure and formation of coals, terrestrial and extraterrestrial kerogens from resonant UV Raman spectroscopy. *Geochimica et Cosmochimica Acta*, *282*, 156–176. https://doi.org/10.1016/j.gca.2020.05.028

Quirico, E., Montagnac, G., Rouzaud, J. N., Bonal, L., Bourot-Denise, M., Duber, S., & Reynard, B. (2009). Precursor and metamorphic condition effects on Raman spectra of poorly ordered carbonaceous matter in chondrites and coals. *Earth and Planetary Science Letters*, *287*(1–2), 185–193. https://doi.org/10.1016/j.epsl.2009.07.041

Razzell Hollis, J. (2024). *Jobium/SaU008: Publication release: Jgr: Planets. 2024/5*. Zenodo. https://doi.org/10.5281/ZENODO.13990660

Razzell Hollis, J., Abbey, W., Beegle, L. W., Bhartia, R., Ehlmann, B. L., Miura, J., et al. (2021). A deep-ultraviolet Raman and fluorescence spectral library of 62 minerals for the SHERLOC instrument onboard Mars 2020. *Planetary and Space Science*, *209*, 105356. https://doi.org/10.1016/j.pss.2021.105356

Razzell Hollis, J., Moore, K. R., Bhartia, R., & Beegle, L. W. (2024). MOBIUS measurements of SaU 008 [Dataset]. *Open Data Reposity*. https://doi.org/10.48484/YY2A-8H26

Razzell Hollis, J., Moore, K. R., Sharma, S., Beegle, L., Grotzinger, J. P., Allwood, A., et al. (2022). The power of paired proximity science observations: Co-located data from SHERLOC and PIXL on Mars. *Icarus*, *387*, 115179. https://doi.org/10.1016/j.icarus.2022.115179

Razzell Hollis, J., Rheingold, D., Bhartia, R., & Beegle, L. W. (2020). An optical model for quantitative Raman microspectroscopy. *Applied Spectroscopy*, *74*(6), 684–700. https://doi.org/10.1177/0003702819895299

Razzell Hollis, J., Sharma, S., Abbey, W., Bhartia, R., Beegle, L., Fries, M., et al. (2023). A deep ultraviolet Raman and fluorescence spectral library of 51 organic compounds for the SHERLOC instrument onboard Mars 2020. *Astrobiology*, *23*(1), 1–23. https://doi.org/10.1089/ast.2022.0023

Scheller, E. L., Bosak, T., McCubbin, F. M., Williford, K., Siljeström, S., Jakubek, R. S., et al. (2024). Inorganic interpretation of luminescent materials encountered by the perseverance rover on Mars. *Science Advances*, *10*(39), eadm8241. https://doi.org/10.1126/sciadv.adm8241

Scheller, E. L., Razzell Hollis, J., Cardarelli, E. L., Steele, A., Beegle, L. W., Bhartia, R., et al. (2022). Aqueous alteration processes in Jezero crater, Mars—Implications for organic geochemistry. *Science*, *378*(6624), 1105–1110. https://doi.org/10.1126/science.abo5204

Schon, S. C., Head, J. W., & Fassett, C. I. (2012). An overfilled lacustrine system and progradational Delta in Jezero crater, Mars: Implications for Noachian climate. *Planetary and Space Science*, *67*(1), 28–45. https://doi.org/10.1016/j.pss.2012.02.003

Sharma, S., Roppel, R. D., Murphy, A. E., Beegle, L. W., Bhartia, R., Steele, A., et al. (2023). Diverse organic-mineral associations in Jezero crater, Mars. *Nature*, *619*(7971), 724–732. https://doi.org/10.1038/s41586-023-06143-z

Shearer, C. K., Burger, P. V., Papike, J. J., McCubbin, F. M., & Bell, A. S. (2015). Crystal chemistry of merrillite from Martian meteorites: Mineralogical recorders of magmatic processes and planetary differentiation. *Meteoritics & Planetary Sciences*, *50*(4), 649–673. https://doi.org/10.1111/maps.12355

Shkolyar, S., Lalla, E., Konstantindis, M., Cote, K., Daly, M. G., & Steele, A. (2021). Detecting Ce3+ as a biosignature mimicker using UV time-resolved laser-induced fluorescence and Raman spectroscopy: Implications for planetary missions. *Icarus*, *354*, 114093. https://doi.org/10.1016/j.icarus.2020.114093

Stack, K. M., Williams, N. R., Calef, F., Sun, V. Z., Williford, K. H., Farley, K. A., et al. (2020). Photogeologic map of the perseverance Rover field site in jezero crater constructed by the Mars 2020 science team. *Space Science Reviews*, *216*(8), 127. https://doi.org/10.1007/s11214-020-00739-x

Steele, A., McCubbin, F. M., Fries, M., Kater, L., Boctor, N. Z., Fogel, M. L., et al. (2012). A reduced organic carbon component in Martian basalts. *Science*, *337*(6091), 212–215. https://doi.org/10.1126/science.1220715

Steele, A., McCubbin, F. M., & Fries, M. D. (2016). The provenance, formation, and implications of reduced carbon phases in Martian meteorites. *Meteoritics & Planetary Sciences*, *51*(11), 2203–2225. https://doi.org/10.1111/maps.12670

Steele, A., McCubbin, F. M., Fries, M. D., Golden, D. C., Ming, D. W., & Benning, L. G. (2012). Graphite in the Martian meteorite Allan Hills 84001. *American Mineralogist*, *97*(7), 1256–1259. https://doi.org/10.2138/am.2012.4148

Toporski, J., & Steele, A. (2007). Observations from a 4-Year contamination study of a sample depth profile through Martian meteorite Nakhla. *Astrobiology*, *7*(2), 389–401. https://doi.org/10.1089/ast.2006.0009

Uckert, K. (2022). Nasa/Loupe: LoupeV5.1.5 (version LoupeV5.1.5a) [Computer software]. *Zenodo*. https://doi.org/10.5281/ZENODO.7062998

Uckert, K., Bhartia, R., Beegle, L. W., Monacelli, B., Asher, S. A., Burton, A. S., et al. (2021). Calibration of the SHERLOC deep ultraviolet fluorescence–raman spectrometer on the perseverance rover. *Applied Spectroscopy*, *75*(7), 763–773. https://doi.org/10.1177/00037028211013368

Uckert, K., Bhartia, R., & Michel, J. (2019). A semi-autonomous method to detect cosmic rays in Raman hyperspectral data sets. *Applied Spectroscopy*, *73*(9), 1019–1027. https://doi.org/10.1177/0003702819850584

Udry, A., Howarth, G. H., Herd, C. D. K., Day, J. M. D., Lapen, T. J., & Filiberto, J. (2020). What Martian meteorites reveal about the interior and surface of Mars. *Journal of Geophysical Research: Planets*, *125*(12), e2020JE006523. https://doi.org/10.1029/2020JE006523

Van Der Walt, S., Schönberger, J. L., Nunez-Iglesias, J., Boulogne, F., Warner, J. D., Yager, N., et al. (2014). Scikit-image: Image processing in python. *PeerJ*, *2*, e453. https://doi.org/10.7717/peerj.453

Virtanen, P., Gommers, R., Oliphant, T. E., Haberland, M., Reddy, T., Cournapeau, D., et al. (2020). SciPy 1.0: Fundamental algorithms for scientific computing in python. *Nature Methods*, *17*(3), 261–272. https://doi.org/10.1038/s41592-019-0686-2

Walton, E. L., Spray, J. G., & Bartoschewitz, R. (2005). A new Martian meteorite from Oman: Mineralogy, petrology, and shock metamorphism of olivine-phyric basaltic shergottite Sayh al Uhaymir 150. *Meteoritics & Planetary Sciences*, *40*(8), 1195–1214. https://doi.org/10.1111/j.1945-5100.2005.tb00184.x

Ward, D., Bischoff, A., Roszjar, J., Berndt, J., & Whitehouse, M. J. (2017). Trace element inventory of meteoritic Ca-phosphates. *American Mineralogist*, *102*(9), 1856–1880. https://doi.org/10.2138/am-2017-6056

Williford, K. H., Farley, K. A., Stack, K. M., Allwood, A. C., Beaty, D., Beegle, L. W., et al. (2018). Chapter 11 - The NASA Mars 2020 rover mission and the search for extraterrestrial life. In N. A. Cabrol & E. A. Grin (Eds.), *From habitability to life on Mars* (pp. 275–308). Elsevier. https://doi.org/10.1016/B978-0-12-809935-3.00010-4

Wogsland, B. V., Minitti, M. E., Kah, L. C., Yingst, R. A., Abbey, W., Bhartia, R., et al. (2023). Science and science-enabling activities of the SHERLOC and WATSON imaging systems in jezero crater, Mars. *Earth and Space Science*, *10*(11), e2022EA002544. https://doi.org/10.1029/2022EA002544

Wright, I. P., Carr, R. H., & Pillinger, C. T. (1986). Carbon abundance and isotopic studies of shergotty and other shergottite meteorites. *Geochimica et Cosmochimica Acta*, *50*(6), 983–991. https://doi.org/10.1016/0016-7037(86)90379-0

Zipfel, J. (2000). Sayh Al Uhaymir 005/008 and its relationship to Dar al Gani 476/489. *Meteoritics & Planetary Sciences*, *35*, A178.